J. Plasma Phys. (2022), *vol*. 88, 905880320
Published by Cambridge University Press
doi:10.1017/S0022377822000605

Density jump as a function of magnetic field for switch-on collisionless shocks in pair plasmas

Antoine Bret [1,2] **and Ramesh Narayan** [3,4,†]

[1]ETSI Industriales, Universidad de Castilla-La Mancha, 13071 Ciudad Real, Spain

[2]Instituto de Investigaciones Energéticas y Aplicaciones Industriales, Campus Universitario de Ciudad Real, 13071 Ciudad Real, Spain

[3]Harvard-Smithsonian Center for Astrophysics, Harvard University, 60 Garden St., Cambridge, MA 02138, USA

[4]Black Hole Initiative at Harvard University, 20 Garden Street, Cambridge, MA 02138, USA

(Received 1 April 2022; revised 14 June 2022; accepted 15 June 2022)

The properties of collisionless shocks, like the density jump, are usually derived from magnetohydrodynamics (MHD), where isotropic pressures are assumed. Yet, in a collisionless plasma, an external magnetic field can sustain a stable anisotropy. We have already devised a model for the kinetic history of the plasma through the shock front (*J. Plasma Phys.*, vol. 84, issue 6, 2018, 905840604), allowing to self-consistently compute the downstream anisotropy, and hence the density jump, in terms of the upstream parameters. This model deals with the case of a parallel shock, where the magnetic field is normal to the front both in the upstream and the downstream. Yet, MHD also allows for shock solutions, the so-called switch-on solutions, where the field is normal to the front only in the upstream. This article consists in applying our model to these switch-on shocks. While MHD offers only one switch-on solution within a limited range of Alfvén Mach numbers, our model offers two kinds of solutions within a slightly different range of Alfvén Mach numbers. These two solutions are most likely the outcome of the intermediate and fast MHD shocks under our model. While the intermediate and fast shocks merge in MHD for the parallel case, they do not within our model. For simplicity, the formalism is restricted to non-relativistic shocks in pair plasmas where the upstream is cold.

Key words: astrophysical plasmas, plasma nonlinear phenomena, space plasma physics

1. Introduction

Shock waves are fundamental processes in plasmas which are usually studied within the context of magnetohydrodynamics (MHD). As an extension of fluid dynamics to plasmas, MHD entails the same assumption of small mean free path (see for example Gurnett & Bhattacharjee 2005, § 5.4.4, Goedbloed, Keppens & Poedts 2010, chaps. 2 and 3 or Thorne & Blandford 2017, § 13.2). When fulfilled, collisions ensure that the pressure is isotropic both in the upstream and downstream, which simplifies the conservation equations.

† Email address for correspondence: antoineclaude.bret@uclm.es

In collisionless shock, where the mean free path is larger than the size of the system, the isotropy assumption may not be fulfilled, possibly resulting in a departure from the MHD predicted behaviour. Such is especially the case in the presence of an external magnetic field which can stabilize a temperature anisotropy, as has been observed in the solar wind (Bale *et al.* 2009; Maruca, Kasper & Bale 2011; Schlickeiser *et al.* 2011) and is projected to be studied in the laboratory (Carter *et al.* 2015).

Some authors worked out the MHD conservation equations in the case of anisotropic pressure and studied the consequences on the shock properties (Erkaev, Vogl & Biernat 2000; Double *et al.* 2004; Gerbig & Schlickeiser 2011). Yet, in these works, while the upstream is assumed isotropic, the downstream degree of anisotropy is left as a free parameter.

Recently, a self-contained theory of magnetized collisionless shocks has been developed. By making some assumptions on the kinetic history of the plasma as it crosses the front, we could compute the downstream degree of anisotropy, for the parallel and the perpendicular cases, in terms of the magnetic field strength (Bret & Narayan 2018, 2019, 2020).

Noteworthily, the theory for parallel shocks described in Bret & Narayan (2018) has been successfully tested against the Particle-In-Cell (PIC) simulations of Haggerty, Bret & Caprioli (2022).

In MHD, several shock solutions exist when the upstream magnetic field is aligned with the flow. The most common solution is the one where the downstream field is also aligned with the flow. This is the fully parallel case, where the fluid and the field are decoupled (Lichnerowicz 1976; Majorana & Anile 1987). Yet, still for the case where the upstream field is parallel to the flow, MHD offers a second option: the switch-on shocks (Kulsrud 2005; Goedbloed *et al.* 2010; Fitzpatrick 2014). In such shocks, while the magnetic field does not have any components along the shock front in the upstream, it has one in the downstream. Indeed, the MHD conservation equations only enforce the continuity of the field component perpendicular to the front, not the continuity of the normal component. Therefore, they allow for solutions, the switch-on solutions, where the upstream field is normal to the front while the downstream field is not.

The theory developed in Bret & Narayan (2018) was the collisionless version of the fully parallel MHD case. The present article deals with the collisionless version of the MHD switch-on shocks.

As in Bret & Narayan (2018), we consider, for simplicity, pair plasmas for which both species have the same perpendicular and parallel temperatures to the field. In § 2, we remember the MHD results for switch-on shocks. In § 3, we explain the method used. It significantly differs from that in Bret & Narayan (2018) since we need to account for an oblique downstream field. In addition, MHD results suggest the obliquity of the downstream field, labelled θ_2 in the following, can be as high as $0.56(\pi/2)$ (see figure 2*a*). We cannot therefore work out a theory restricted to $\theta_2 = \varepsilon$, with $0 < \varepsilon \ll 1$. Then, in §§ 4 and 5, we explain the solutions found for switch-on shocks within our model.

2. MHD results

The system considered is sketched in figure 1. The upstream field $\boldsymbol{B}_1$ and velocity $\boldsymbol{v}_1$ are normal to the front, but the downstream ones $\boldsymbol{B}_2$ and $\boldsymbol{v}_2$ are not. They make an angle θ_2 and ξ_2 with the shock normal and by default, $\theta_2 \neq \xi_2$ (even though they will be found equal in the following).

We here briefly remember the MHD theory for switch-on shocks. Due to the complexity of the forthcoming calculations, we treat only the case of a sonic strong shock, namely upstream temperature $T_1 = 0$, or equivalently, upstream sonic Mach number $\mathcal{M}_{s1} = \infty$.

https://doi.org/10.1017/S0022377822000605 Published online by Cambridge University Press

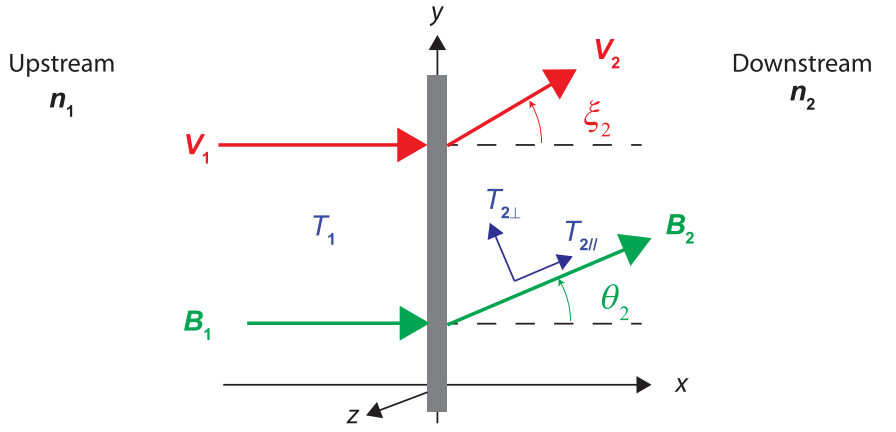

FIGURE 1. System considered. The upstream has density n_1 and isotropic temperature T_1. Both the upstream field $\boldsymbol{B}_1$ and velocity $\boldsymbol{v}_1$ are normal to the front. The downstream has density n_2 and temperatures $T_{2\parallel}$, $T_{2\perp}$, parallel and perpendicular to the downstream field, respectively. The downstream field $\boldsymbol{B}_2$ and velocity $\boldsymbol{v}_2$ make an angle θ_2 and ξ_2, respectively, with the front normal. The parallel and perpendicular directions are therefore defined with respect to the local magnetic field.

For isotropic pressures in the upstream and the downstream, and $\theta_1 = \xi_1 = 0$, the MHD conservation equations for strong shock and an adiabatic index of $\gamma = 5/3$ read (see for example Kulsrud 2005, p. 141)

$$n_2 v_2 \cos\xi_2 = n_1 v_1, \tag{2.1}$$

$$B_2 \cos\theta_2 = B_1, \tag{2.2}$$

$$B_2 v_2 \sin\theta_2 \cos\xi_2 - B_2 v_2 \cos\theta_2 \sin\xi_2 = 0, \tag{2.3}$$

$$\frac{B_2^2 \sin^2\theta_2}{8\pi} + n_2 k_B T_2 + m n_2 v_2^2 \cos^2\xi_2 = m n_1 v_1^2, \tag{2.4}$$

$$m n_2 v_2^2 \sin\xi_2 \cos\xi_2 - \frac{B_2^2 \sin\theta_2 \cos\theta_2}{4\pi} = 0, \tag{2.5}$$

$$m n_2 v_2 \cos\xi_2 \left(\frac{5}{2}\frac{k_B T_2}{m} + \frac{B_2^2 \sin^2\theta_2}{4\pi m n_2} + \frac{v_2^2}{2}\right) - \frac{B_2^2}{4\pi} v_2 \sin\theta_2 \cos\theta_2 \sin\xi_2 = \frac{1}{2} m n_1 v_1^3, \tag{2.6}$$

where m is the mass of the particles and k_B the Boltzmann constant.

Equation (2.1) stands for the conservation of mass. Equation (2.2) for the conservation of the magnetic field normal component. Equation (2.3) for the vanishing of the z component of the electric field. Equations (2.4) and (2.5) come from the conservation of the momentum flux (see Appendix A), and (2.6) from the conservation of energy.

By eliminating v_2 and B_2 thanks to (2.1) and (2.2), and then eliminating T_2 thanks to (2.4), the system is amenable to three equations,

$$\tan\theta_2 - \tan\xi_2 = 0, \tag{2.7}$$

$$\mathcal{M}_{A1}^2 \tan\xi_2 - r\tan\theta_2 = 0, \tag{2.8}$$

$$2\mathcal{M}_{A1}^2[(r-5)r + 5 - \sec^2\xi_2] + r\tan\theta_2\,(\tan\theta_2 + 4\tan\xi_2) = 0, \tag{2.9}$$

https://doi.org/10.1017/S0022377822000605 Published online by Cambridge University Press

in terms of the dimensionless density ratio r and the Alfvén Mach number $\mathcal{M}_{A1}$,

$$\left.\begin{aligned} r &= \frac{n_2}{n_1}, \\ \mathcal{M}_{A1}^2 &= \frac{mn_1 v_1^2}{B_1^2/4\pi}. \end{aligned}\right\} \tag{2.10}$$

The first equation imposes $\theta_2 = \xi_2$. Replacing in the last two gives

$$\tan\theta_2(\mathcal{M}_{A1}^2 - r) = 0, \tag{2.11}$$

$$2\mathcal{M}_{A1}^2[(r-5)r + 5 - \sec^2\theta_2] + 5r\tan^2\theta_2 = 0. \tag{2.12}$$

Equation (2.11) clearly defines two kinds of shocks.

(i) The first kind comes from $\tan\theta_2 = 0$, that is, $\theta_2 = 0$. Inserting it into (2.12) gives $r = 1$ or $r = 4$. The first option, $r = 1$, is the continuity solution, where nothing changes between the upstream and the downstream. The second option is the parallel shock solution, with $r = 4$ for a sonic strong shock and an adiabatic index $\gamma = 5/3$.

(ii) Yet, (2.11) also allows for

$$r = \mathcal{M}_{A1}^2, \tag{2.13}$$

which is the MHD switch-on solution. Inserting it into (2.12) gives

$$\cos^2\theta_2 = \frac{3}{10\mathcal{M}_{A1}^2 - 2\mathcal{M}_{A1}^4 - 5}. \tag{2.14}$$

The value of θ_2 so defined is displayed in figure 2(*a*). Here, $\theta_2 \neq 0$ is only permitted within a finite range of Alfvén Mach numbers defined by $\cos^2\theta_2 < 1$, that is, $1 < \mathcal{M}_{A1} < 2$. Note that instead of parametrizing θ_2 by the Alfvén Mach number $\mathcal{M}_{A1}$, we choose the variable

$$\sigma = \frac{B_1^2/4\pi}{mn_1 v_1^2} = \frac{1}{\mathcal{M}_{A1}^2}. \tag{2.15}$$

This σ parameter allows for a straightforward comparison with PIC simulations where σ is usually used instead of $\mathcal{M}_{A1}$ (see for example Sironi & Spitkovsky 2011; Bret 2020). As a function of σ, $\theta_2 \neq 0$ is allowed for $\sigma \in [1/4, 1]$.

For a finite upstream temperature $T_1 > 0$, MHD switch-on solutions are also restricted to a range of upstream temperatures via $\beta_1 = n_1 k_B T_1/B_1^2 < 2/\gamma$, where γ is the adiabatic index (Kennel, Blandford & Coppi 1989; de Sterck & Poedts 1999; Delmont & Keppens 2011). (See in particular figure 3 in de Sterck & Poedts (1999).) Since the present work is limited to $T_1 = 0$, it cannot explore this dimension of the switch-on solutions range.

While they have been produced in the laboratory (Craig & Paul 1973), such shocks have been rarely detected in space due to the smallness of the parameter window that allows them. Feng *et al.* (2009) reported the detection of a 'possible' interplanetary switch-on shock. Also, Farris *et al.* (1994); Russell & Farris (1995) reported the detection of one switch-on shock among the ISEE (International Sun-Earth Explorer; see Ogilvie, Rosenvinge & Durney (1977)) data. The more recent review by Balogh & Treumann (2013) still refers to the results of Farris *et al.* (1994) as 'the rare case of observation of a switch-on shock' in its § 2.3.6.

Finally, it is interesting to compute the MHD density jump r for any upstream angle θ_1. This can be done solving the 'shock adiabatic' equation given in Fitzpatrick (2014, § 7.21),

https://doi.org/10.1017/S0022377822000605 Published online by Cambridge University Press

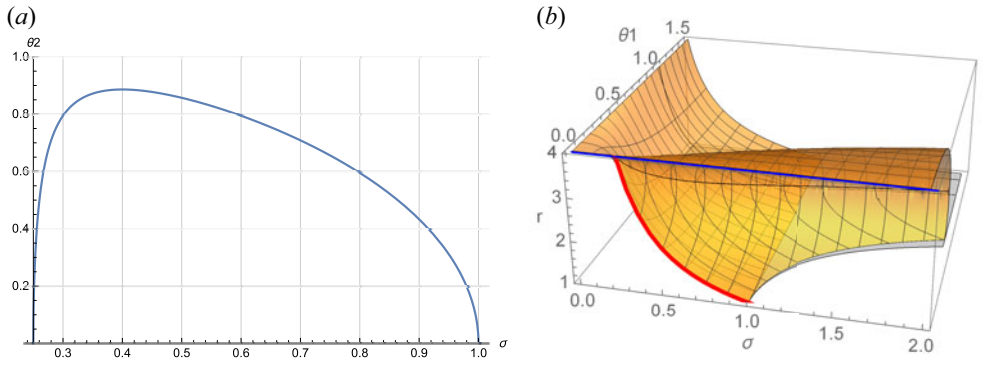

FIGURE 2. (*a*) Value of θ_2 from (2.14) in terms of $\sigma = \mathcal{M}_{A1}^{-2}$. Its maximum value is $\arccos\sqrt{2/5} \sim 0.56(\pi/2)$. (*b*) MHD density jump r in terms of (σ, θ_1) for $\theta_1 \in [0, \pi/2]$. Only the blue line, which has $\theta_1 = \theta_2 = 0$, was considered in Bret & Narayan (2018). The red line is the switch-on solution (2.13), with $\theta_1 = 0$ but $\theta_2 \neq 0$.

and setting $T_1 = 0$. ($V_{S1} = 0$ in the notation of Fitzpatrick (2014).) The result is pictured in figure 2(*b*), in terms of $\theta_1 \in [0, \pi/2]$ and σ. Only the blue line, which has $\theta_1 = \theta_2 = 0$, was considered in Bret & Narayan (2018). The red line is the switch-on solution (2.13), with $\theta_1 = 0$ but $\theta_2 \neq 0$.

3. Method

Our method to determine the downstream anisotropy in terms of the upstream field relies on a monitoring of the kinetic history of the plasma as it crosses the front. In this process, the parallel and perpendicular temperatures of the plasma are changed according to some prescriptions explained below. The resulting state of the plasma downstream is labelled 'Stage 1.' Stage 1 is generally not isotropic.

Depending on the strength of the downstream field $\boldsymbol{B}_2$, Stage 1 can be stable or not. If it is stable, then Stage 1 is the end state of the downstream. If it is unstable, then the plasma migrates towards its instability threshold, namely mirror or firehose stability. This is 'Stage 2.' In such a case, Stage 2 is the end state of the downstream.

Stages 1 and 2 are therefore temporal evolving stages of the downstream plasma. This has been verified for the parallel case by the PIC simulations performed by Haggerty *et al.* (2022), where the two stages have been clearly identified.

Also, the stability alluded here is not the one of the whole shock structure, like for example the corrugation instability (Landau & Lifshitz 2013, § 90). It is rather the stability of the downstream plasma as an isolated and homogeneous entity.

This algorithm was applied to the parallel and perpendicular cases in Bret & Narayan (2018) and Bret & Narayan (2019), respectively. In both cases, the orientation of $\boldsymbol{B}_2$ makes it simple to set the temperatures of Stage 1. We will now see that the obliquity of $\boldsymbol{B}_2$ demands further characterization of Stage 1.

3.1. *Characterization of Stage 1*

If the motion of the plasma through the front were adiabatic, the corresponding evolution of the parallel and perpendicular temperatures would be described by the double adiabatic

https://doi.org/10.1017/S0022377822000605 Published online by Cambridge University Press

Cases	$T_{2\parallel}$	$T_{2\perp}$
Parallel, $\theta_{1,2}=0$	$T_1\left(\frac{n_2B_1}{n_1B_2}\right)^2+\text{entropy}$	$T_1\frac{B_1}{B_2}$
Perpendicular, $\theta_{1,2}=\pi/2$	$T_1\left(\frac{n_2B_1}{n_1B_2}\right)^2$	$T_1\frac{B_1}{B_2}+\text{entropy}$

TABLE 1. Values of $T_{2\parallel}$ and $T_{2\perp}$ in Stage 1 for the parallel and perpendicular cases.

equations of Chew, Goldberger & Low (1956):

$$\left.\begin{aligned}\frac{T_\parallel B^2}{n^2}&=cst,\\ \frac{T_\perp}{B}&=cst.\end{aligned}\right\} \tag{3.1}$$

Here, like in the rest of the paper, the parallel and perpendicular are defined with respect to the local magnetic field.

Now, since we are dealing with shockwaves, the evolution of the plasma from the upstream to the downstream is not adiabatic. For parallel and perpendicular shocks, this results in different prescriptions.

(i) For the parallel shock case treated in Bret & Narayan (2018), we took $\theta_{1,2}=\xi_{1,2}=0$ and considered the entropy excess goes into the parallel temperature. Intuitively, this stems from the fact that the transit of the plasma through the front can be viewed as a compression between two converging virtual walls, normal to the flow. These walls by no means exist. They are simply an analogy of how the entropy gain is realized. Regarding the perpendicular temperature, (3.1) simply gives $T_\perp=cst$ in the parallel case, since $B_2=B_1$ for such a shock. Such changes of the temperatures have been successfully checked through PIC simulations by Haggerty *et al.* (2022).

(ii) For the perpendicular shock case treated in Bret & Narayan (2019), we took $\theta_{1,2}=\pi/2$ and $\xi_{1,2}=0$. Here the plasma can still be viewed as compressed between two virtual walls normal to the flow. We therefore considered that the temperature normal to the flow, that is, parallel to the field, evolves adiabatically.

An additional constraint that must always be satisfied is the equality of the two temperatures perpendicular to the field, enforced by the Vlasov equation (Landau & Lifshitz 1981, § 53).

These considerations are summarized in table 1 which gives the values of $T_{2\parallel}$ and $T_{2\perp}$ in the parallel and perpendicular cases.

As already stated in § 1, MHD suggests that in a switch-on shock, the obliquity θ_2 of the downstream field can be as high as $0.56\frac{\pi}{2}$. Hence, we need to interpolate between the two extremes of table 1. We cannot just elaborate from Bret & Narayan (2018) by exploring $\theta_2=\varepsilon$, with $0<\varepsilon\ll 1$.

https://doi.org/10.1017/S0022377822000605 Published online by Cambridge University Press

For intermediate values of θ_2, we propose the following interpolation between the two extremes of table 1:

$$\left.\begin{aligned} T_{2\parallel} &= T_1\left(\frac{n_2 B_1}{n_1 B_2}\right)^2 + T_e\cos^2\theta_2, \\ T_{2\perp} &= T_1\frac{B_1}{B_2} + \frac{1}{2}T_e\sin^2\theta_2. \end{aligned}\right\} \tag{3.2}$$

Our *ansatz* is therefore that the downstream temperatures are the sum of the adiabatic ones given by Chew *et al.* (1956), plus an entropy excess. For the parallel temperature, the entropy excess is a fraction $\cos^2\theta_2$ of a quantity we label T_e (subscript 'e' for entropy). For the perpendicular temperature, the entropy excess is a fraction $\sin^2\theta_2/2$ of the same T_e. Here, the factor $1/2$ accounts for the necessary identity of the two perpendicular temperatures. Finally, the three temperature excesses sum to T_e.

The $\cos^2\theta_2$ and $\sin^2\theta_2$ functions are the simplest choice fulfilling these requirements. Further works, notably PIC simulations (see § 6), should allow to test their relevance.

Note that T_e is not arbitrary but is solved for using the conservation equations (see (B6) in Appendix B). It represents the heat generated from the shock entropy.

We now compute the properties of Stage 1 accounting for these extended prescriptions for Stage 1.

4. Properties of Stage 1

Due to the complexity of the calculations, we treat only the case of a sonic strong shock, namely $T_1 = 0$.

4.1. *Conservation equations for anisotropic temperatures*

The conservation equations for anisotropic temperatures in the downstream are established in Appendix A. Though with different notation, they can be found in Hudson (1970); Erkaev *et al.* (2000). With $T_1 = 0$, they read,

$$n_2 v_2\cos\xi_2 = n_1 v_1, \tag{4.1}$$

$$B_2\cos\theta_2 = B_1, \tag{4.2}$$

$$B_2 v_2\sin\theta_2\cos\xi_2 - B_2 v_2\cos\theta_2\sin\xi_2 = 0, \tag{4.3}$$

$$\cos^2\theta_2 n_2 k_B T_{2\parallel} + \sin^2\theta_2 n_2 k_B T_{2\perp} + m n_2 v_2^2\cos^2\xi_2 - \frac{B_2^2\cos(2\theta_2)}{8\pi} = -\frac{B_1^2}{8\pi} + m n_1 v_1^2, \tag{4.4}$$

$$\sin\theta_2\cos\theta_2 n_2 k_B(T_{2\parallel} - T_{2\perp}) + m n_2 v_2^2\sin\xi_2\cos\xi_2 - \frac{B_2^2\sin(2\theta_2)}{8\pi} = 0, \tag{4.5}$$

$$[v\,(\mathcal{A}\cos\xi + \mathcal{B}\cos\xi + \mathcal{C}\sin\xi)]_1^2 = 0, \tag{4.6}$$

where

$$\left.\begin{aligned} \mathcal{A} &= \frac{1}{2}n k_B T_\parallel + n k_B T_\perp + \frac{B^2}{8\pi} + \frac{1}{2}m n v^2, \\ \mathcal{B} &= -\frac{B^2\cos(2\theta)}{8\pi} + \cos^2\theta\, n k_B T_\parallel + \sin^2\theta\, n k_B T_\perp, \\ \mathcal{C} &= \sin\theta\cos\theta\, n k_B\left(T_\parallel - T_\perp\right) - \frac{B^2\sin(2\theta)}{8\pi}. \end{aligned}\right\} \tag{4.7}$$

https://doi.org/10.1017/S0022377822000605 Published online by Cambridge University Press

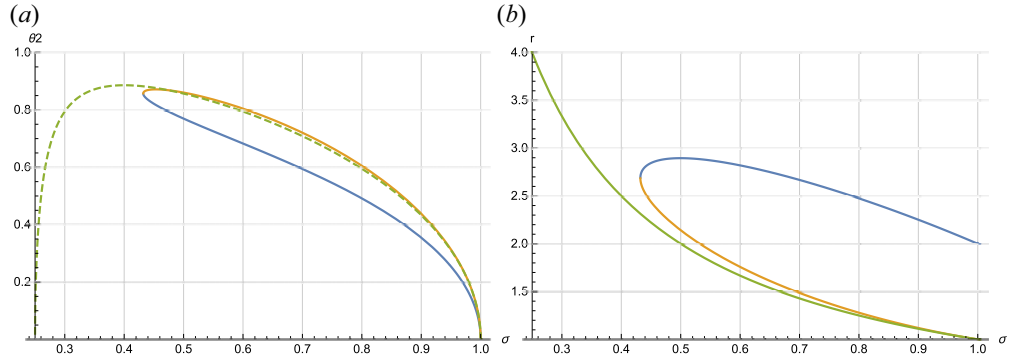

FIGURE 3. (*a*) Values of θ_2 arising from $Q = 0$ in (B11). Solutions exist only for $\sigma \in [0.432, 1]$. (*b*) Corresponding values of the density jump from (B10). The colour code refers to the corresponding θ_2-branch. The green curves pertain to the MHD switch-on solution.

In (4.6), the notation $[Q]_1^2$ stands for the difference of any quantity Q between the upstream and the downstream.

With $T_1 = 0$, prescriptions (3.2) for the downstream temperatures in Stage 1 simply read

$$\left.\begin{aligned} T_{2\parallel} &= T_e \cos^2\theta_2, \\ T_{2\perp} &= \frac{1}{2} T_e \sin^2\theta_2. \end{aligned}\right\} \tag{4.8}$$

4.2. *Resolution of the system of equations*

The resolution of the system (4.1)–(4.8) is lengthy and reported in Appendix B. It turns out that it is convenient to determine first the angle θ_2 as a function of σ, and then to compute the density jump $r(\sigma)$.

The algebra unravels three θ_2-branches for $\theta_1 = 0$.

(i) One branch is simply $\theta_2 = 0$, with $r = 1$ and $r = 2$. The first one, with $r = 1$, is the continuity solution. The second one, with $r = 2$, is the parallel strong sonic shock solution for Stage 1, already studied in Bret & Narayan (2018).

(ii) The other branch defines two values of $\theta_2(\sigma)$ which correspond to our switch-on solutions. They are pictured in figure 3(*a*). Then the corresponding density jump $r(\sigma)$ is computed and plotted in figure 3(*b*). The green curve pictures the MHD switch-on solution (2.13), defined for $\sigma \in [1/4, 1]$. In Stage 1, numerical exploration shows solutions exist only for $\sigma \in [0.432, 1]$.
Therefore, while there is only one switch-on solution in MHD, our model offers two. Figure 3(*a*) shows that both of our branches merge with the MHD result for $\sigma = 1$ as far as θ_2 is concerned. Such is only the case for the lower of our r-branch, as can be seen from figure 3(*b*).

Figure 3(*a*) shows that the largest value of θ_2 in Stage 1 is almost as high as its MHD counterpart.

In accordance with the method explained in § 3, we now study the stability of Stage 1.

https://doi.org/10.1017/S0022377822000605 Published online by Cambridge University Press

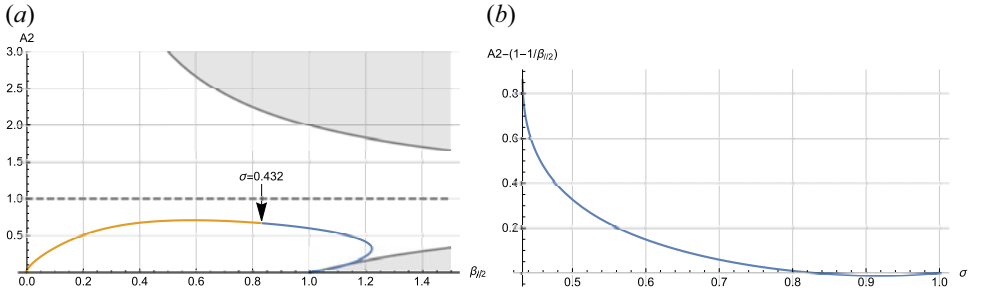

FIGURE 4. (*a*) Thresholds for the mirror (upper grey line) and firehose (lower grey line) instabilities. The plasma is unstable within the shaded areas. The loop shows the curves $(\beta_{\parallel 2}(\sigma), A_2(\sigma))$ for the two θ_2-branches defined previously. The two branches start from the same point for $\sigma = 0.432$, and both reach $A_2 = 0$ for $\sigma = 1$. (*b*) Stability analysis of the blue branch for $\sigma \in [0.432, 1]$. It is found firehose unstable for $\sigma \in [0.82, 1]$.

4.3. *Stability of Stage 1*

If unstable, Stage 1 is mirror or firehose unstable. The thresholds for these instabilities are given by (Gary 1993; Gary & Karimabadi 2009)

$$\frac{T_{2\perp}}{T_{2\parallel}} \equiv A_2 = 1 \pm \frac{1}{\beta_{\parallel 2}}, \tag{4.9}$$

where

$$\beta_{\parallel 2} = \frac{n_2 k_B T_{2\parallel}}{B_2^2/(8\pi)}, \tag{4.10}$$

and the '+' and '−' signs stand for the thresholds of the mirror and firehose instabilities, respectively. From (4.8), we obtain the downstream anisotropy A_2,

$$A_2 = \tfrac{1}{2}\tan^2\theta_2. \tag{4.11}$$

For $\beta_{\parallel 2}$, we obtain, in Appendix C,

$$\beta_{\parallel 2} = -2\frac{r\sigma\tan^2\theta_2 - 2r + 2}{r\sigma(\tan^4\theta_2 + 2)}. \tag{4.12}$$

To assess the stability of Stage 1, we then proceed as follows.

(i) From (4.9), we plot the thresholds for the mirror and firehose instabilities in the $(\beta_{\parallel 2}, A_2)$ plane.
(ii) Then, on the same graph, we plot the curves $(\beta_{\parallel 2}, A_2)$ for the two non-trivial θ_2-branches found in § 4.2.

The result is pictured in figure 4(*a*). In Bret & Narayan (2018), Stage 1 had $A_2 = 0$ for the sonic strong shock case. Here, A_2 departs from 0 but remains small.

It turns out that the orange branch pictured in figure 3(*a*), namely the one closest to the MHD solution, is stable for any σ. Yet, the blue one is slightly unstable in some σ range. For this branch, the quantity $A_2 - (1 - \beta_{\parallel 2}^{-1})$ is plotted in figure 4(*b*). It is negative for $\sigma \in [0.83, 1]$, indicating firehose instability. In this σ-range, the downstream will therefore migrate to Stage 2, on the firehose threshold.

https://doi.org/10.1017/S0022377822000605 Published online by Cambridge University Press

As can be seen in figure 4(*a*), the blue branch Stage 1 is only slightly unstable. Consequently, the corresponding marginally stable Stage 2 is very close to the unstable states. This is confirmed below in § 5, where Stage 2 is analysed.

For now, to document the differences between our two branches, we further study Stage 1 by computing its entropy and its Alfvénic downstream velocity.

4.4. *Entropy of Stage 1*

The two branches for Stage 1 cannot be distinguished by their energy since they both fulfil the energy conservation equation (4.6), where the upstream energy is the same in both cases. Their energy densities are therefore identical. Yet, they can be distinguished on the basis of their entropy.

For a bi-Maxwellian of the form,

$$F = \frac{n}{\pi^{3/2}\sqrt{ab}} \exp\left(-\frac{v_x^2}{a}\right) \exp\left(-\frac{v_y^2+v_z^2}{b}\right), \tag{4.13}$$

where $a = 2k_B T_\parallel/m$ and $b = 2k_B T_\perp/m$, the entropy reads

$$S = -k_B \int F \ln F d^3v = \frac{1}{2} k_B n[3 + \ln(\pi^3 ab^2) - 2\ln n], \tag{4.14}$$

where $n = \int F d^3v$. Using the subscript 'b' for the blue branch in figure 3, and subscript 'o' for the orange one, we get for the entropy difference per particle between the two branches,

$$\begin{aligned}
\frac{2}{k_B}\left(\frac{S_o}{n_o} - \frac{S_b}{n_b}\right) \equiv \Delta s &= \ln\left[\frac{a_o b_o^2}{a_b b_b^2}\right] + 2\ln\frac{n_b}{n_o}, \\
&= \ln\left[\frac{T_{\parallel 2,o}\, T_{\perp 2,o}^2}{T_{\parallel 2,b}\, T_{\perp 2,b}^2}\right] + 2\ln\frac{n_b}{n_o}, \\
&= \ln\left[\frac{T_{\parallel 2,o}^3 A_{2,o}^2}{T_{\parallel 2,b}^3 A_{2,b}^2}\right] + 2\ln\frac{n_b}{n_o}, \\
&= \ln\left[\left(\frac{T_{e,o}\cos^2\theta_{2,o}}{T_{e,b}\cos^2\theta_{2,b}}\right)^3 \frac{A_{2,o}^2}{A_{2,b}^2}\right] + 2\ln\frac{n_b}{n_o},
\end{aligned} \tag{4.15}$$

where we have used $A_2 = T_{\perp 2}/T_{\parallel 2}$ and then $T_{\parallel 2} = T_e \cos^2\theta_2$ for both branches.

The numerical evaluation (T_e is given by (B6)) of this quantity displayed in figure 5(*a*) shows that $\Delta s < 0$ for any $\sigma \in [0.432, 1]$. Therefore, $S_o/n_o < S_b/n_b$ for any σ. The orange branch in figure 3 has lower entropy than the blue one.

4.5. *Downstream Alfvénic Mach number of Stage 1*

Another difference between the two branches lies in their respective Alfvénic Mach number, namely,

$$\mathcal{M}_{A2}^2 = \frac{m n_2 v_2^2}{B_2^2/4\pi}. \tag{4.16}$$

From (4.2), we get $B_2 = B_1/\cos\theta_2$. Then (4.1) gives $v_2 = n_1 v_1/n_2 \cos\xi_2 = n_1 v_1/n_2 \cos\theta_2$, since $\xi_2 = \theta_2$ in our model as in MHD (see (2.7) for MHD and Appendix B for our model).

https://doi.org/10.1017/S0022377822000605 Published online by Cambridge University Press

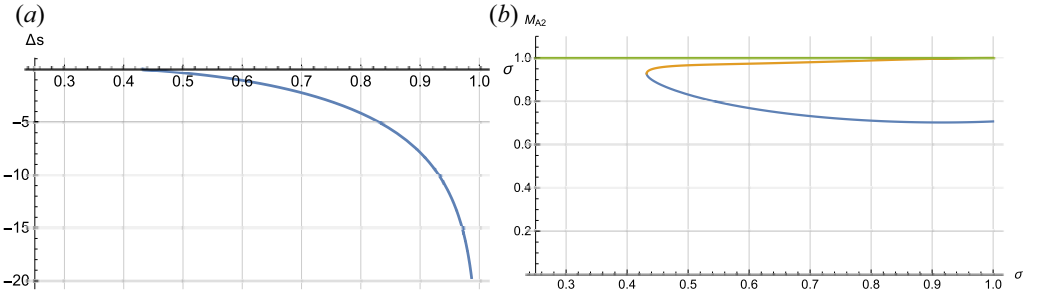

FIGURE 5. (*a*) Entropy difference Δs as defined by (4.15), between the blue branch in figure 3 and the orange one. Here, $\Delta s < 0$ implies the orange branch has lower entropy than the blue one. (*b*) Value of $\mathcal{M}_{A2}$ in MHD (green) and for the two branches of our model.

We finally obtain, in terms of the dimensionless variables (2.10), with both our model and MHD,

$$\mathcal{M}_{A2} = \frac{\mathcal{M}_{A1}}{\sqrt{r}} = \frac{1}{\sqrt{\sigma r}}. \tag{4.17}$$

(i) In MHD, (2.13) has $r = \mathcal{M}_{A1}^2$, so that for the switch-on MHD shock, $\mathcal{M}_{A2} = 1$ (Goedbloed *et al.* 2010, p. 853).

(ii) In our model, the value of $\mathcal{M}_{A2}$ is pictured in figure 5(*b*) for the two branches represented in figure 3. Our two branches are found slightly sub-Alfvénic.

5. Properties of Stage 2

The firehose instability of the blue branch for $\sigma \in [0.83, 1]$ requires studying the properties of Stage 2 when marginally firehose stable. The conservation equations are the same. However, instead of imposing prescriptions (3.2) for the temperatures, we now impose firehose marginal stability for the downstream, namely,

$$\frac{T_{2\perp}}{T_{2\parallel}} = 1 - \frac{1}{\beta_{\parallel 2}}. \tag{5.1}$$

The resolution of the system follows the same path as that described in Appendix B for Stage 1. It yields three equations for θ_2, ξ_2 and r,

$$\tan\theta_2 - \tan\xi_2 = 0, \tag{5.2}$$

$$\frac{2\tan\xi_2}{r} - \frac{\tan\theta_2}{\mathcal{M}_{A1}^2} = 0, \tag{5.3}$$

$$\mathcal{M}_{A1}^2(-\sec^2\xi_2 + (r-5)r + 5) + r\tan\theta_2\tan\xi_2 + r = 0. \tag{5.4}$$

Equation (5.2) imposes again $\theta_2 = \xi_2$. Replacing in (5.3) gives

$$\tan\theta_2(r - 2\mathcal{M}_{A1}^2) = 0, \tag{5.5}$$

which leaves two options only.

(i) $\theta_2 = 0$, which pertains to the parallel shock solution. Setting then $\theta_2 = 0$ in (5.4) then gives exactly the Stage 2 solution found in Bret & Narayan (2018). (See (3.5) of Bret & Narayan (2018) for $\chi_1 = \infty$.)

https://doi.org/10.1017/S0022377822000605 Published online by Cambridge University Press

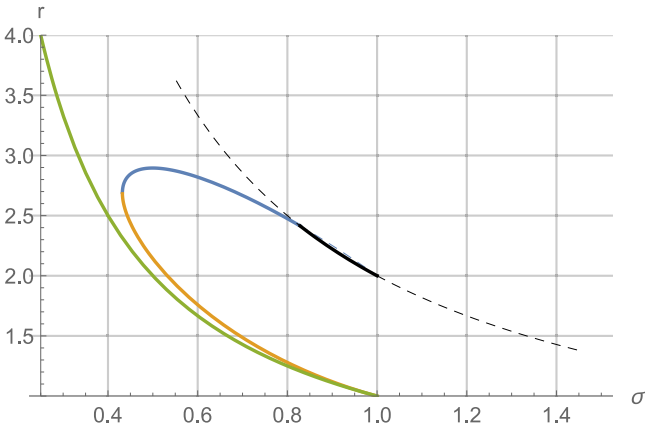

FIGURE 6. Same as figure 3(*b*) but showing how Stages 1 and 2 fit together when accounting for the firehose instability of the blue branch for $\sigma \in [0.83, 1]$. Stage 2 density jump $r = 2/\sigma$ is discontinued from $\sigma = 1$ since Stage 1 has no solution in this range.

(ii) The other option is,

$$r = 2\mathcal{M}_{A1}^2 = 2/\sigma. \tag{5.6}$$

Inserting this result in (5.4) and solving for θ_2 gives

$$\cos^2\theta_2 = \frac{1}{10\mathcal{M}_{A1}^2 - 4\mathcal{M}_{A1}^4 - 5}, \tag{5.7}$$

reminiscent of (2.14) for the MHD case. Solutions can here be found for

$$\left.\begin{aligned} \mathcal{M}_{A1} &\in \left[\frac{\sqrt{5-\sqrt{5}}}{2}, \frac{\sqrt{5+\sqrt{5}}}{2}\right] \sim [0.83, 1.34], \\ \Leftrightarrow \sigma = \frac{1}{\mathcal{M}_{A1}^2} &\in \left[\frac{4}{5+\sqrt{5}}, \frac{4}{5-\sqrt{5}}\right] \sim [0.55, 1.44]. \end{aligned}\right\} \tag{5.8}$$

The counterpart to switch-on shock is therefore recovered in our model for Stage 2 as well, still in a limited range of Alfvén Mach numbers.

Figure 6 is eventually the end result of the present work. Like figure 3(*b*), it features the density jump of the MHD switch-on solution, together with the two branches of our model. However here, the way Stages 1 and 2 fit together in the σ unstable range is elucidated. Since the blue branch has been found firehose unstable for $\sigma \in [0.83, 1]$, it is replaced by Stage 2, namely (5.6), in this range. As expected, the corresponding density jump is very close to that of Stage 1 since the system is almost marginally stable in this range, while Stage 2 sits exactly on marginal stability.

In figure 6, the jump for Stage 2, namely $r = 2/\sigma$, is shown in black and plotted within the full range (5.8) where it is defined. For $\sigma < 0.83$, the line is dashed because Stage 1 is stable, and hence defines the density jump. Then for $\sigma \in [0.83, 1]$, the blue branch is dashed since it pertains to the unstable Stage 1. There, the jump is now given by Stage 2 through $r = 2/\sigma$. Beyond $\sigma = 1$, Stage 1 offers no solutions. Since in our scenario Stage 1 is the first state of the downstream after crossing the front, the shock cannot accommodate such values of σ in the switch-on regime. For $\sigma > 1$, there is therefore

https://doi.org/10.1017/S0022377822000605 Published online by Cambridge University Press

no Stage 1 from where the system could jump to Stage 2, even though Stage 2 offers solutions. As a consequence, the black curve is dashed from $\sigma = 1$ to 1.44.

6. Conclusion

In a collisionless non-magnetized plasma, the Weibel instability ensures isotropy, since it makes anisotropies unstable (Weibel 1959; Silva, Afeyan & Silva 2021). Therefore, for collisionless shocks in such medium, the only source of departures from MHD should stem from accelerated particles (Bret 2020; Haggerty & Caprioli 2020).

In contrast, a temperature anisotropy can be stabilized in a collisionless plasma by an external magnetic field. Therefore, if the plasma turns anisotropic when crossing the front of a collisionless shock, its downstream anisotropy could be stable, resulting in a departure from MHD.

Several authors studied the conservation equations for a shock accounting for anisotropic pressures. Yet, the downstream degree of anisotropy is considered a free parameter in these works (Erkaev *et al.* 2000; Double *et al.* 2004; Gerbig & Schlickeiser 2011). In the present article, we devised a model allowing to compute the degree of anisotropy of the downstream, in terms of the upstream parameters. We focused on the switch-on solutions where the field is aligned with the flow in the upstream, but not in the downstream.

For such a configuration, MHD allows for one shock solution, the switch-on solution, for which the density jump is given by (2.13). According to our model, which has been successfully tested against PIC simulations for the parallel case (Haggerty *et al.* 2022), there are two collisionless switch-on solutions for which the angle θ_2 and the density jump r are plotted in figures 3 and 6. One solution for what we named 'Stage 1' is stable for any σ where it is defined. The other is slightly firehose unstable within a limited σ-range. Exploring then Stage 2 in this range allows to correct the computed density jump. Since the Stage 1 that needed to be corrected was only slightly firehose unstable, the correction found with Stage 2 marginally firehose stable is small.

The existence of two switch-on solutions in our model instead of one in MHD could be explained. We plotted in figure 2(*b*) the MHD solutions for a cold upstream and any upstream field obliquity θ_1. One can see that the MHD switch-on solution for $\theta_1 = 0$ splits into two different solutions for $\theta_1 > 0$. These two solutions are the intermediate and fast shocks. They merge for $\theta_1 = 0$, which is why MHD switch-on shocks can be termed intermediate or fast (Goedbloed *et al.* 2010, p. 853).

Possibly within our model, these two kinds of shocks do not merge for $\theta_1 = 0$. Future works dealing with the fully oblique case $\theta_1 > 0$ will explore how the MHD intermediate and fast shocks morph within our model.

Is one of our two branches physically favoured? Both pertain to a downstream plasma with the same energy density since both fulfil the energy conservation equation (4.6) where the upstream term is the same. We see from figures 3 and 5 that the orange one is the closest to the MHD solution, yet we found in § 4.4 that it has lower entropy than the blue branch. Further works, notably PIC simulations, would be needed to find out if these two branches are just our model's version of the oblique intermediate and fast shocks in the limit $\theta_1 = 0$.

In the same way that the theory devised for the parallel case has been tested through PIC simulation (Bret & Narayan 2018; Haggerty *et al.* 2022), it would be interesting to test the present conclusions through the same means. Yet, to our knowledge, no PIC simulations of switch-on shocks have been performed to date (Sironi & Lembège 2022). An option in this respect would be to reproduce in PIC the bow shock MHD simulation performed by de Sterck & Poedts (1999). There, it was found that a portion of the bow shock produced

https://doi.org/10.1017/S0022377822000605 Published online by Cambridge University Press

by the simulation was of the switch-on type. Possibly a PIC counterpart of this work would allow to produce a switch-on shock and study it at the kinetic scale.

Acknowledgements

Thanks are due to L. Sironi and B. Lembège for enriching discussions.

Editor Luís O. Silva thanks the referees for their advice in evaluating this article.

Funding

A.B. acknowledges support by grants PID2021-127322OB-I00 from the Spanish Ministerio de Economía y Competitividad. R.N. acknowledges support from the NSF Grant No. AST- 1816420. R.N. thanks the Black Hole Initiative (BHI) at Harvard University for support. The BHI is funded by grants from the John Templeton Foundation and the Gordon and Betty Moore Foundation.

Declaration of interests

The authors report no conflict of interest.

Appendix A. Derivation of the conservation equations for anisotropic temperatures

Equations (4.1)–(4.3) are identical to their MHD counterparts since they do not involve the pressure. The differences due to anisotropic pressure are rather to be found in (4.4)–(4.6). For (4.4) and (4.5), we start from the momentum flux density tensor equation (Landau & Lifshitz 2013, § 7),

$$\frac{\partial(\rho v_i)}{\partial t} = -\frac{\partial \Pi_{ik}}{\partial x_k}. \tag{A1}$$

In the shock frame, the left-hand side vanishes. Using the basis x, y, z represented in figure 1, where the shock jump is in the x direction, we obtain the following jump conditions:

$$[\Pi_{xx}]_1^2 = \left[\Pi_{xy}\right]_1^2 = 0, \tag{A2}$$

where the notation $[Q]_1^2$ stands for the difference of any quantity Q between the upstream and the downstream.

There are three contributions to the tensor Π_{ik}: ram pressure, magnetic pressure and thermal pressure.

(i) The ram pressure part reads

$$\Pi_{\rm ram} = \begin{pmatrix} nmv^2\cos^2\xi & nmv^2\cos\xi\sin\xi & 0 \\ nmv^2\cos\xi\sin\xi & nmv^2\sin^2\xi & 0 \\ 0 & 0 & 0 \end{pmatrix}, \tag{A3}$$

where all quantities are to be taken with subscript 1 for the upstream and 2 for the downstream.

(ii) For the magnetic pressure, we start in a basis (x', y', z') aligned with the field. In such a basis,

$$\Pi'_{\rm mag} = \begin{pmatrix} -B^2/8\pi & 0 & 0 \\ 0 & B^2/8\pi & 0 \\ 0 & 0 & B^2/8\pi \end{pmatrix}. \tag{A4}$$

https://doi.org/10.1017/S0022377822000605 Published online by Cambridge University Press

We now express this tensor in our basis (x, y, z), where $z = z'$ and (x', y') are rotated by an angle θ. Hence, we compute $R^{-1}\Pi'_{\mathrm{mag}}R$, with

$$R = \begin{pmatrix} \cos\theta & \sin\theta & 0 \\ -\sin\theta & \cos\theta & 0 \\ 0 & 0 & 1 \end{pmatrix}. \tag{A5}$$

The result is

$$\Pi_{\mathrm{mag}} = \frac{B^2}{8\pi}\begin{pmatrix} -\cos 2\theta & -\sin 2\theta & 0 \\ -\sin 2\theta & \cos 2\theta & 0 \\ 0 & 0 & 1 \end{pmatrix}. \tag{A6}$$

(iii) The calculation is similar for the thermal pressure. We start in a basis adapted to the field,

$$\Pi'_{\mathrm{th}} = nk_B\begin{pmatrix} T_\parallel & 0 & 0 \\ 0 & T_\perp & 0 \\ 0 & 0 & T_\perp \end{pmatrix}, \tag{A7}$$

where the directions $\parallel$ and $\perp$ are considered with respect to the field. Computing $R^{-1}\Pi'_{\mathrm{th}}R$, where the tensor R is still given by (A5), gives, in our basis (x, y, z),

$$\Pi_{\mathrm{th}} = nk_B\begin{pmatrix} T_\parallel\cos^2\theta + T_\perp\sin^2\theta & (T_\parallel - T_\perp)\cos\theta\sin\theta & 0 \\ (T_\parallel - T_\perp)\cos\theta\sin\theta & T_\parallel\sin^2\theta + T_\perp\cos^2\theta & 0 \\ 0 & 0 & T_\perp \end{pmatrix}. \tag{A8}$$

When adding the contributions (A3), (A6) and (A8), the conservation (A2) yields (4.4) and (4.5).

For the last equation, namely (4.6), we start from the energy conservation equation (Landau & Lifshitz 2013, § 6),

$$\frac{\partial}{\partial t}\left(\frac{1}{2}nmv^2 + \varepsilon_{\mathrm{mag}} + \varepsilon_{\mathrm{th}}\right) = -\frac{\partial}{\partial x_k}\left[v_k\left(\frac{1}{2}nmv^2 + \varepsilon_{\mathrm{mag}} + \varepsilon_{\mathrm{th}}\right)\right] - \frac{\partial}{\partial x_k}\left[v_i\left(\Pi_{ik,\mathrm{mag}} + \Pi_{ik,\mathrm{th}}\right)\right], \tag{A9}$$

where ε is the internal energy density,

$$\varepsilon_{\mathrm{mag}} = \frac{B^2}{8\pi}, \tag{A10}$$

$$\varepsilon_{\mathrm{th}} = \frac{1}{2}nk_BT_\parallel + nk_BT_\perp, \tag{A11}$$

and Π_{mag}, Π_{th} are given by (A6) and (A8), respectively. Setting the left-hand side of (A9) to 0, and equating the right-hand side between the upstream and the downstream, gives (4.6).

Appendix B. Resolution of the system (4.1)–(4.8)

The system (4.1)–(4.8) can be reduced to a system of three equations for $r \equiv n_2/n_1$, θ_2 and T_e. The pathway to do so is as follows.

https://doi.org/10.1017/S0022377822000605 Published online by Cambridge University Press

(i) We first notice that (4.3) imposes $\xi_2 = \theta_2$ (as in MHD). We can therefore set $\xi_2 = \theta_2$ everywhere.
(ii) We then use (4.1) to eliminate v_2 everywhere.
(iii) Next, we use (4.2) to eliminate B_2 everywhere.

At this junction, we are left with three equations which are the updated versions of (4.4)–(4.6). They read

$$r^2\overline{T_e}\sin^4\theta_2 + 2r^2\overline{T_e}\cos^4\theta_2 + r\sigma\tan^2\theta_2 - 2r + 2 = 0, \tag{B1}$$

$$r^2\overline{T_e}\,[2\sin(2\theta_2) + 3\sin(4\theta_2)] + 16\tan\theta_2(1 - r\sigma) = 0, \tag{B2}$$

$$\sec^2\theta_2 + r^2\left[\overline{T_e}\cos(2\theta_2) + 2\overline{T_e} - 1\right] = 0, \tag{B3}$$

in terms of the density ratio r and the magnetic parameter σ defined in (2.15), plus

$$\overline{T_e} = \frac{k_B T_e}{m v_1^2}. \tag{B4}$$

For further progress, it is convenient to define

$$X_2 = \arcsin\theta_2. \tag{B5}$$

This change of variables makes the forthcoming equations polynomial in X_2 easy to solve numerically. The value of $\overline{T_e}$ can be extracted from (B1) and reads

$$\overline{T_e} = \frac{r[(\sigma+2)X_2^2 - 2] - 2X_2^2 + 2}{r^2(X_2^2-1)(X_2^2(3X_2^2-4)+2)}. \tag{B6}$$

Substituting it in (B2) and (B3) yields the two equations,

$$X_2\underbrace{\left[r\left\{\sigma(4 + 3(X_2^2-2)X_2^2) - 6X_2^4 + 10X_2^2 - 4\right\} - 2X_2^2\right]}_{\equiv\Lambda} = 0, \tag{B7}$$

$$\sum_{k=0}^{3} a_k X_2^{2k}, = 0, \tag{B8}$$

with

$$\left.\begin{aligned} a_0 &= 2(r-2)(r-1),\\ a_1 &= r(-6r + 3\sigma + 10) - 6,\\ a_2 &= 7r^2 - 2(\sigma+2)r + 1,\\ a_3 &= -3r^2. \end{aligned}\right\} \tag{B9}$$

Equation (B7) clearly displays two branches.

(i) One branch is $X_2 = 0$, that is, $\theta_2 = 0$. Inserting it into (B8) gives $a_0 = 0$, that is, $r = 1$ or $r = 2$. The first one, with $r = 1$, is the continuity solution. The second one, with $r = 2$, is the parallel strong sonic shock solution for Stage 1, already studied in Bret & Narayan (2018).

https://doi.org/10.1017/S0022377822000605 Published online by Cambridge University Press

(ii) The second branch pertains to $\Lambda = 0$. We can extract the value of r from $\Lambda = 0$, namely,

$$r = \frac{2X_2^2}{\sigma[3(X_2^2-2)X_2^2+4] - 6X_2^4 + 10X_2^2 - 4}, \tag{B10}$$

and substitute in (B8). This eventually gives a polynomial equation for X_2 only, which reads

$$Q(X_2) = \sum_{k=0}^{4} b_k X_2^{2k}, \tag{B11}$$

with

$$\left.\begin{aligned} b_0 &= 32\sigma^2 - 64\sigma + 32, \\ b_1 &= -80\sigma^2 + 200\sigma - 120, \\ b_2 &= 76\sigma^2 - 224\sigma + 160, \\ b_3 &= -30\sigma^2 + 100\sigma - 84, \\ b_4 &= 3\sigma^2 - 12\sigma + 12. \end{aligned}\right\} \tag{B12}$$

It can be solved numerically and gives the two values of $\theta_2(\sigma) = \arcsin X_2(\sigma)$ plotted in figure 3(*a*). Solutions exist only for $\sigma \in [0.432, 1]$. Then (B10) allows to compute the density jump r for each θ_2-branch and plot them in figure 3(*b*).

Appendix C. Calculation of $\beta_{\parallel 2}$

We need to evaluate

$$\beta_{\parallel 2} = \frac{n_2 k_B T_{2\parallel}}{B_2^2/(8\pi)}. \tag{C1}$$

Equation (4.2) gives $B_2 = B_1/\cos\theta_2$. Also, (4.8) gives $T_{2\parallel} = T_e \cos^2\theta_2$. Finally, (B6) gives T_e. Expressing the result in terms of the dimensionless variables r and σ yields (4.12) for $\beta_{\parallel 2}$.

REFERENCES

Bale, S.D., Kasper, J.C., Howes, G.G., Quataert, E., Salem, C. & Sundkvist, D. 2009 Magnetic fluctuation power near proton temperature anisotropy instability thresholds in the solar wind. *Phys. Rev. Lett.* **103**, 211101.

Balogh, A. & Treumann, R.A. 2013 *Physics of Collisionless Shocks: Space Plasma Shock Waves*. Springer.

Bret, A. 2020 Can we trust MHD jump conditions for collisionless shocks? *Astrophys. J.* **900** (2), 111.

Bret, A. & Narayan, R. 2018 Density jump as a function of magnetic field strength for parallel collisionless shocks in pair plasmas. *J. Plasma Phys.* **84** (6), 905840604.

Bret, A. & Narayan, R. 2019 Density jump as a function of magnetic field for collisionless shocks in pair plasmas: the perpendicular case. *Phys. Plasmas* **26** (6), 062108.

Bret, A. & Narayan, R. 2020 Density jump for parallel and perpendicular collisionless shocks. *Laser Part. Beams* **38** (2), 114–120.

Carter, T., Dorfman, S., Gekelman, W., Tripathi, S., van Compernolle, B., Vincena, S., Rossi, G. & Jenko, F. 2015 Studies of the linear and nonlinear properties of Alfvén waves in LAPD. In *APS Division of Plasma Physics Meeting Abstracts, APS Meeting Abstracts*, vol. 2015, p. GM9.006.

https://doi.org/10.1017/S0022377822000605 Published online by Cambridge University Press

Chew, G.F., Goldberger, M.L. & Low, F.E. 1956 The Boltzmann equation and the one-fluid hydromagnetic equations in the absence of particle collisions. *Proc. R. Soc. Lond.* A **236** (1204), 112–118.

Craig, A.D. & Paul, J.W.M. 1973 Observation of 'switch-on' shocks in a magnetized plasma. *J. Plasma Phys*. **9** (2), 161–186.

Delmont, P. & Keppens, R. 2011 Parameter regimes for slow, intermediate and fast MHD shocks. *J. Plasma Phys*. **77** (2), 207–229.

Double, G.P., Baring, M.G., Jones, F.C. & Ellison, D.C. 2004 Magnetohydrodynamic jump conditions for oblique relativistic shocks with gyrotropic pressure. *Astrophys. J*. **600**, 485.

Erkaev, N.V., Vogl, D.F. & Biernat, H.K. 2000 Solution for jump conditions at fast shocks in an anisotropic magnetized plasma. *J. Plasma Phys*. **64**, 561–578.

Farris, M.H., Russell, C.T., Fitzenreiter, R.J. & Ogilvie, K.W. 1994 The subcritical, quasi-parallel, switch-on shock. *Geophys. Res. Lett*. **21** (9), 837–840.

Feng, H.Q., Lin, C.C., Chao, J.K., Wu, D.J., Lyu, L.H. & Lee, L.C. 2009 Observations of an interplanetary switch-on shock driven by a magnetic cloud. *Geophys. Res. Lett*. **36**, L07106.

Fitzpatrick, R. 2014 *Plasma Physics: An Introduction*. Taylor & Francis.

Gary, S.P. 1993 *Theory of Space Plasma Microinstabilities*. Cambridge University Press.

Gary, S.P. & Karimabadi, H. 2009 Fluctuations in electron-positron plasmas: linear theory and implications for turbulence. *Phys. Plasmas* **16** (4), 042104.

Gerbig, D. & Schlickeiser, R. 2011 Jump conditions for relativistic magnetohydrodynamic shocks in a gyrotropic plasma. *Astrophys. J*. **733** (1), 32.

Goedbloed, J.P., Keppens, R. & Poedts, S. 2010 *Advanced Magnetohydrodynamics: With Applications to Laboratory and Astrophysical Plasmas*. Cambridge University Press.

Gurnett, D.A. & Bhattacharjee, A. 2005 *Introduction to Plasma Physics: With Space and Laboratory Applications*. Cambridge University Press.

Haggerty, C.C., Bret, A. & Caprioli, D. 2022 Kinetic simulations of strongly magnetized parallel shocks: deviations from MHD jump conditions. *Mon. Not. R. Astron. Soc*. **509** (2), 2084–2090.

Haggerty, C.C. & Caprioli, D. 2020 Kinetic simulations of cosmic-ray-modified shocks. I. Hydrodynamics. *Astrophys. J*. **905** (1), 1.

Hudson, P.D. 1970 Discontinuities in an anisotropic plasma and their identification in the solar wind. *Planet. Space Sci*. **18** (11), 1611–1622.

Kennel, C.F., Blandford, R.D. & Coppi, P. 1989 MHD intermediate shock discontinuities. Part 1. Rankine–Hugoniot conditions. *J. Plasma Phys*. **42** (2), 299–319.

Kulsrud, R.M. 2005 *Plasma Physics for Astrophysics*. Princeton University Press.

Landau, L.D. & Lifshitz, E.M. 1981 *Course of Theoretical Physics, Physical Kinetics*, vol. 10. Elsevier.

Landau, L.D. & Lifshitz, E.M. 2013 *Fluid Mechanics*. Elsevier Science.

Lichnerowicz, A. 1976 Shock waves in relativistic magnetohydrodynamics under general assumptions. *J. Math. Phys*. **17** (12), 2135–2142.

Majorana, A. & Anile, A.M. 1987 Magnetoacoustic shock waves in a relativistic gas. *Phys. Fluids* **30**, 3045–3049.

Maruca, B.A., Kasper, J.C. & Bale, S.D. 2011 What are the relative roles of heating and cooling in generating solar wind temperature anisotropies? *Phys. Rev. Lett*. **107**, 201101.

Ogilvie, K.W., Rosenvinge, T.V. & Durney, A.C. 1977 International sun-earth explorer – 3-spacecraft program. *Science* **198** (4313), 131–138.

Russell, C.T. & Farris, M.H. 1995 Ultra low frequency waves at the earth's bow shock. *Adv. Space Res*. **15** (8–9), 285–296.

Schlickeiser, R., Michno, M.J., Ibscher, D., Lazar, M. & Skoda, T. 2011 Modified temperature-anisotropy instability thresholds in the solar wind. *Phys. Rev. Lett*. **107**, 201102.

Silva, T., Afeyan, B. & Silva, L.O. 2021 Weibel instability beyond bi-Maxwellian anisotropy. *Phys. Rev.* E **104** (3), 035201.

Sironi, L. & Lembège, B. 2022 *private communication*.

Sironi, L. & Spitkovsky, A. 2011 Particle acceleration in relativistic magnetized collisionless electron-ion shocks. *Astrophys. J*. **726**, 75.

DE STERCK, H. & POEDTS, S. 1999 Field-aligned magnetohydrodynamic bow shock flows in the switch-on regime. Parameter study of the flow around a cylinder and results for the axi-symmetrical flow over a sphere. *Astron. Astrophys*. **343**, 641–649.

THORNE, K.S. & BLANDFORD, R.D. 2017 *Modern Classical Physics: Optics, Fluids, Plasmas, Elasticity, Relativity, and Statistical Physics*. Princeton University Press.

WEIBEL, E.S. 1959 Spontaneously growing transverse waves in a plasma due to an anisotropic velocity distribution. *Phys. Rev. Lett*. **2**, 83.